Oxygen delivery using engineered microparticles

Raymond P. Seekell[a,b], Andrew T. Lock[a], Yifeng Peng[a,b], Alexis R. Cole[a], Dorothy A. Perry[a,b], John N. Kheir[a,b], and Brian D. Polizzotti[a,b,1]

[a]Division of Basic Cardiovascular Research, Department of Cardiology, Boston Children's Hospital, Boston, MA 02115; and [b]Department of Pediatrics, Harvard Medical School, Boston, MA 02115

Edited by Howard A. Stone, Princeton University, Princeton, NJ, and approved September 13, 2016 (received for review May 25, 2016)

A continuous supply of oxygen to tissues is vital to life and interruptions in its delivery are poorly tolerated. The treatment of low-blood oxygen tensions requires restoration of functional airways and lungs. Unfortunately, severe oxygen deprivation carries a high mortality rate and can make otherwise-survivable illnesses unsurvivable. Thus, an effective and rapid treatment for hypoxemia would be revolutionary. The i.v. injection of oxygen bubbles has recently emerged as a potential strategy to rapidly raise arterial oxygen tensions. In this report, we describe the fabrication of a polymer-based intravascular oxygen delivery agent. Polymer hollow microparticles (PHMs) are thin-walled, hollow polymer microcapsules with tunable nanoporous shells. We show that PHMs are easily charged with oxygen gas and that they release their oxygen payload only when exposed to desaturated blood. We demonstrate that oxygen release from PHMs is diffusion-controlled, that they deliver approximately five times more oxygen gas than human red blood cells (per gram), and that they are safe and effective when injected in vivo. Finally, we show that PHMs can be stored at room temperature under dry ambient conditions for at least 2 mo without any effect on particle size distribution or gas carrying capacity.

hypoxemia | microparticle | oxygen | core–shell | colloids

A continuous supply of oxygen is necessary to maintain human life, with healthy adults consuming ~3 mL $O_2 \cdot kg^{-1} \cdot min^{-1}$ (i.e., 200 mL O_2/min for 70-kg adult) (1, 2). Interruptions in oxygen delivery are poorly tolerated, leading to cellular injury and apoptosis within minutes. However, the treatments for patients with a life-threatening degree of oxygen deprivation are all dependent on an intact and functioning airway–lung unit. When institution of these measures is delayed or ineffective, due to impaired airway–lung function or lack of access to specialized equipment and personnel, patients suffer organ dysfunction, cardiac arrest, or death within minutes. Strategies that enable i.v. injection of oxygen gas would provide a therapeutic approach to rapidly raise blood oxygen tensions and may serve as a bridge therapy until advanced life support can be implemented. However, despite more than a century of research, the safe and effective i.v. delivery of oxygen gas has not been realized (3–5).

There are several theoretical approaches to rapidly increasing arterial oxygen content in the setting of an emergency. The most obvious may be directly bubbling oxygen gas into the bloodstream, although this approach is impractical due to the low solubility of oxygen in plasma and the occurrence of intravascular bubble coalescence. Historically, direct infusion of free oxygen gas into the blood stream has resulted in pulmonary emboli at extremely low infusion rates (i.e., 0.25 mL$\cdot kg^{-1} \cdot min^{-1}$, corresponding to only 8% of measured oxygen consumption of a healthy human adult) (4, 6). Other groups have proposed the use of supersaturated oxygen suspensions to increase oxygen content of injected fluids, although even when the pO_2 reaches ~1,000 mmHg, solutions only deliver ~1 mL $O_2 \cdot kg^{-1} \cdot h^{-1}$ in vivo (7). Another theoretical approach would be to use artificial oxygen carriers to deliver dissolved oxygen to the bloodstream. Hemoglobin-based carriers contain hemoglobin or synthetic heme analogs, which reversibly bind dissolved oxygen in response to concentration gradients (8–10). Perfluorocarbon (PFC)-based carriers dissolve large quantities of oxygen within their liquid cores and deliver it to tissues by passive diffusion (11, 12). However, when the lungs are incapable of reoxygenating these carriers, the volume load required and by-products produced to continually administer more oxygen to the bloodstream quickly becomes prohibitive. In addition, challenges with heme toxicity (13), poor control over oxygen binding affinities (14), and PFC-induced microvascular vasoconstriction (15) make these systems poorly suited for rapid i.v. oxygen therapy.

One potential solution to this problem is to use a gas-stabilizing agent to contain the oxygen gas and to prevent bubble coalescence during and following injection (16–19). From a theoretical perspective, this approach is preferred as it overcomes the concentration limits of dissolved or bound oxygen. Our group first demonstrated the feasibility of this approach by packaging oxygen gas within lipid-coated microbubbles (LOMs) (17). Similar to microbubble-based contrast agents, LOMs consist of an oxygen gas core stabilized by a lipid shell. Oxygen transport across the shell occurs via passive diffusion and is triggered when the bubble encounters blood with low oxygen tensions (i.e., relative to the oxygen-rich LOM core, pO_2 < 740 mmHg) (16–18). Because LOMs contain large gas volume fractions [i.e., >70% (vol/vol)], they can deliver substantially larger gas payloads than other particle-based systems that use hemoglobin, heme derivatives, or PFCs. In fact, i.v. infusion of LOMs rapidly raised arterial blood saturations and decreased the incidence of death in several animal models of severe hypoxemia (17, 20). However, despite the effectiveness of lipid-based stabilizing agents, several challenges must be addressed before clinical translation. First, the fluid nature of lipid shells renders LOMs mechanically fragile and introduces the possibility of rupture during rapid injections, releasing free gas to the bloodstream. Second, LOMs, like other lipid-based carriers, are susceptible to coalescence, Ostwald ripening, and Laplace overpressure during storage (21, 22), which leads to significant product loss and undesirable changes in size distributions (17). Design strategies that reduce the risk of free gas release, and improve the drug shelf life while preserving a high oxygen carrying capacity,

Significance

The clinical treatment of profound oxygen deprivation (hypoxemia) is time sensitive and requires skill and specialized equipment. When the airways or lungs become incapacitated (e.g., due to airway obstruction or lung injury), resuscitation is ineffective until oxygenation is restored. Many critically ill patients suffer organ dysfunction, cardiac arrest, or death within minutes. In this work, we describe a polymeric microparticle-based oxygen delivery technology capable of rapidly administering large volumes of oxygen gas through an intravenous line.

Author contributions: R.P.S., A.T.L., Y.P., J.N.K., and B.D.P. designed research; R.P.S., A.T.L., Y.P., A.R.C., D.A.P., and B.D.P. performed research; R.P.S., J.N.K., and B.D.P. analyzed data; and R.P.S. and B.D.P. wrote the paper.

The authors declare no conflict of interest.

This article is a PNAS Direct Submission.

[1]To whom correspondence should be addressed. Email: brian.polizzotti@cardio.chboston.org.

This article contains supporting information online at www.pnas.org/lookup/suppl/doi:10.1073/pnas.1608438113/-/DCSupplemental.

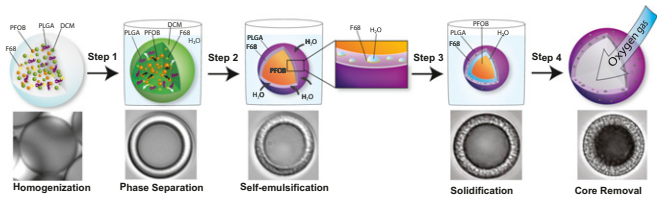

Fig. 1. Schematic representation of the phase separation/self-emulsification strategy used to fabricate PHMs with highly tunable shell properties. A DCM solution containing PLGA (shell material), PFOB (nonsolvent), and Pluronic F-68 (self-emulsifying agent) is homogenized in water to yield stable dispersions. (Step 1) As the droplet solvent (DCM) diffuses into the aqueous phase, the nonsolvent (PFOB) phase separates to form a droplet with a core–shell structure. (Step 2) The aqueous phase diffuses into the DCM-rich droplet, which, in the presence of F-68, results in the spontaneous formation of water-in-oil (w/o) nanoemulsions within the PLGA-rich shell phase. Control over the precipitation rate of the PLGA governs the extent of pore formation. (Step 3) The droplets are allowed to ripen overnight to harden the PLGA shell. (Step 4) Freeze-drying yields gas-filled particles, suggesting that a fraction of the pores coalesced during fabrication to yield a network of capillary channels within the shell. Time-lapse photomicrographs showing the production of PHMs are shown underneath each schematic.

rapid release kinetics, appropriate size distributions, and safety profile of LOMs, would be highly desirable.

Here, we report our strategy toward the development of a class of intravascular gas delivery agents: polymer-based hollow microparticles (PHMs). Unlike LOMs, PHMs are not bubbles; rather, they are thin-walled, hollow microcapsules with a tunable nanoporous shell composed of biodegradable polymers. The primary advantage of PHMs is the mechanical stability imparted by the polymer shell, which should allow them to be filtered, rapidly infused through a syringe, and stored as freeze-dried powders for several months. The latter is particularly important because it preserves the gas carrying capacity and size distribution of the PHMs. Another advantage of PHMs is the nanoporous shell, which should enable loading and release of oxygen gas from PHM powders by passive diffusion. This is desirable because it allows PHMs to be fabricated from hydrophobic biosorbable polymers, like poly(D,L-lactic-coglycolic) acid (PLGA), with intrinsically low oxygen permeabilities (23).

Results and Discussion

To test our gas carrier design, we established a method to fabricate PHMs with tunable shell properties. We developed a two-stage, emulsion-based approach that uses a phase separation step to generate core–shell particles followed by a spontaneous self-emulsification step that results in the formation of an interconnected porous network within the shell structure. PLGA was chosen as the shell material because of its documented use in the medical device and pharmaceutical industry and for its ability to form core–shell structures using phase separation (24, 25). To manufacture PHMs, PLGA (shell material), perfluorooctyl bromide (nonsolvent) (PFOB) and Pluronic F-68 (self-emulsifying agent) were dissolved in dicholoromethane (common solvent) (DCM) and emulsified in an aqueous solution [0.5 wt% polyvinylppyrrolidone (PVP)] to produce an oil-in-water emulsion (Fig. 1). The emulsion was subsequently diluted with distilled water and allowed to ripen. During the ripening process, solvent exchange occurs in which DCM diffuses into the aqueous phase and is ultimately removed from the solution by evaporation. As the DCM is removed, the concentration of the remaining excipients increases, which drives phase separation of the PFOB from the PLGA/F-68 (Fig. 1, step 1). The resultant droplet adopts a core–shell geometry with PFOB-rich cores and PLGA/F-68–rich shells (Fig. 1, step 2). Simultaneously, the aqueous phase diffuses into the droplet, which, in the presence of F-68, results in the spontaneous formation of water-in-oil (w/o) nanoemulsions within the PLGA-rich shell phase (Fig. 1, step 2 *Inset*). This is due to F-68's ability to form reverse micelles, which drastically increases the solubility of water in DCM (26). In the absence of F-68, the poor solubility of water in DCM limits the extent to which this process occurs ($S_{H2O\ in\ DCM}$ = 0.2 wt%; Fig. S1). The emulsion is stirred overnight to completely remove the DCM and to harden the PHM shell (Fig. 1, step 3). Because water vapor easily permeates through PLGA, subsequent freeze-drying of the particles with embedded nanoemulsions yields gas-filled PHMs (Fig. 1, step 4). This suggests that a fraction of the pores are interconnected and span the entire shell thickness, whereas those with solid PLGA shells (i.e., no F-68) yield PFOB-filled microparticles (Fig. S1).

We were able to manipulate particle size, shell thickness, pore density, and pore diameter by controlling homogenization speed and precipitation rate of the PLGA [by changing the dilution factor (DF)]. As a proof of concept, we manufactured four PHM formulations for further testing (Table S1). For example, PHMs fabricated at 2,000 rpm (Silverson Machines, Inc.; East Longmeadow, MA; model: L5M-A), followed by slow (DF = 86, formulation 1; Fig. 2 *A* and *B*) or rapid (DF = 150, formulation 2; Fig. 2 *C* and *D*) precipitation, yielded PHMs with mean diameters (d) of ~8.5 ± 0.24 and 9.3 ± 0.29 μm (Fig. 2*E*) and shell thicknesses (δ) of 2.3 ± 1.0 and 1.1 ± 0.60 μm (Fig. 2*F*, $P < 0.0001$), respectively. The percentage of PHMs greater than 10 μm was 34.0 ± 1.0% and 43.2 ± 1.9%, respectively. Interestingly, rapid precipitation (DF = 150) of the PLGA trapped the nanoemulsions within the shell, whereas slow precipitation (DF = 86) provided time for the intramural nanoemulsions to coalesce into microemulsions. The resultant porous shells had mean diameters of 0.24 ± 0.03 and 1.4 ± 0.2 μm (Fig. 2*G*, $P < 0.0001$) and pore densities of 6.5 ± 0.7 and 0.3 ± 0.03 pores per μm^2 (Fig. 2*H*, $P < 0.0001$), respectively. It is important to emphasize that, in the latter case, the shell is primarily composed of a single layer of large pores with micrometer-sized surface defects (Fig. 2 *A* and *B*). Increasing the homogenization speed results in

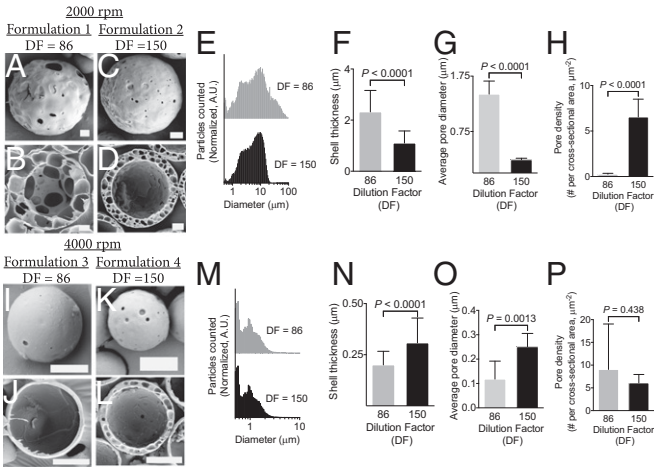

Fig. 2. Control over particle morphology and size is achieved by manipulating the processing parameters. (*A–D*) Homogenization at 2,000 rpm (Silverson Machines, Inc.; East Longmeadow, MA; model: L5M-A) followed by low (*A* and *B*) or high (*C* and *D*) dilutions altered the precipitation rate of the PLGA shell to generate PHMs with varying internal morphologies. (*E*) Lower DFs increased the polydispersity of PHMs fabricated at slow homogenization speeds. (*F–H*) Lower DFs lead to PHMs with thicker shells (*F*) and larger pore diameters (*G*), but decreased pore densities (*H*), compared with higher dilutions. (*I–L*) Homogenization at 4,000 rpm (Silverson Machines, Inc.; East Longmeadow, MA; model: L5M-A) followed by slow (*I* and *J*) or fast (*K* and *L*) precipitation rates. (*M*) Increased homogenization speed reduced the polydispersity of PHMs, regardless of DF. (*N–P*) Lower DFs produce PHMs with thinner shells and smaller pore diameters, but similar pore densities as higher dilutions. [Scale bars: 10 μm (*A–D*); 2 μm (*I–L*).]

particles with smaller mean diameters and thinner shells, regardless of the DF (formulation 3, DF = 86; Fig. 2 *I* and *J*; formulation 4, DF = 150; Fig. 2 *K* and *L*). More specifically, homogenization at 4,000 rpm (Silverson Machines, Inc.; East Longmeadow, MA; model: L5M-A) followed by slow or rapid precipitation, yielded PHMs with mean diameters of 3.3 ± 0.84 and 1.3 ± 0.99 μm (Fig. 2*M*) and shell thicknesses of 0.2 ± 0.07 and 0.31 ± 0.12 μm (Fig. 2*N*, $P < 0.0001$), respectively. The percentage of PHMs greater than 10 μm was 0.1 ± 0.03% and 0.7 ± 0.20%, respectively. Again, rapid precipitation trapped the spontaneously formed nanoemulsions within the shell, resulting in PHMs with similar pores diameters (DF = 150, 0.25 ± 0.05 μm; Fig. 2*O*) and densities (DF = 150, 6.1 ± 0.65 pores/μm^2; Fig. 2*P*) as their thicker-shelled counterparts. However, because the pore diameter (0.25 ± 0.05 μm) is similar to the shell thickness (0.31 ± 0.12 μm), only a single layer of pores can be formed (Fig. 2*L*). In contrast, slow precipitation of thin-shelled PHMs allowed the nanoemulsions to migrate to the core where they coalesced into a large water droplet that encapsulated the PFOB phase (Fig. S2). The continued influx of water into the emulsion caused the droplets to swell until the PLGA completely hardened. The resultant PHMs had significantly thinner shells (0.20 ± 0.07 μm; Fig. 2*N*, $P < 0.001$) and smaller pore diameters (0.12 ± 0.07 μm; Fig. 2*O*, $P = 0.0013$) but similar pore densities (Fig. 2*P*, $P > 0.05$) as rapidly precipitated PHMs.

Next, we characterized the rehydration behavior of PHMs. Swelling and differential scanning calorimetry experiments indicated that PHMs absorb two times their mass in water (Fig. 3*A*) and the PLGA shell plasticizes within minutes of rehydration at 37 °C (T_{gPHMs} = 38–40 °C vs. T_{gPLGA} 55 °C; Fig. 3*B*). To visualize rehydration, we prepared monolayer films of air-filled PHMs on glass coverslips and monitored their behavior using time-lapse optical microscopy. Rehydration of freeze-dried PHMs with air-saturated water at 37 °C produces a suspension of gas-filled particles, as evidenced by the appearance of a dark core under optical microscopy

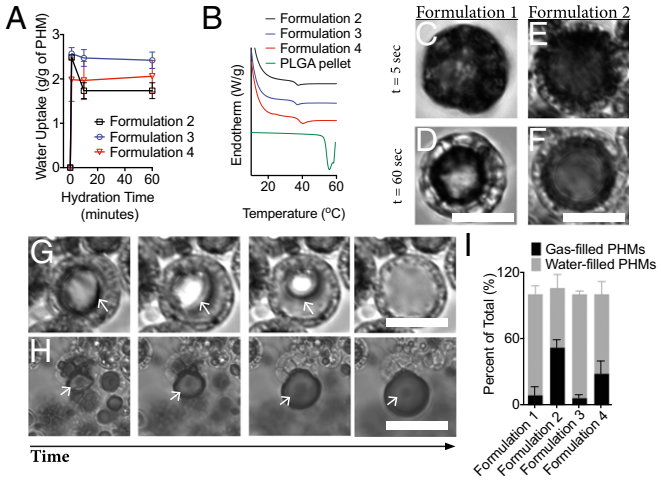

Fig. 3. Rapid rehydration of the PLGA shell and hydrophilic capillary networks mediate gas release from PHMs. (*A*) PHMs rapidly absorb two times their weight in water within minutes of rehydration. (*B*) Rehydration plasticizes the PLGA shell and reduces its T_g from 55 °C to 38–40 °C for formulations 1–4. (*C*–*F*) Within seconds of rehydration, water is wicked into the shell's capillary network leading to the formation of multiple gas–water interfaces. PHM cores appear black due to refraction of light under optical microscopy. (*G* and *H*) On longer timescales, wicking drives dissolution of the gas core (*G*) when the surface pores are less than 250 nm and free gas release (*H*) when the pores exceed 1.4 μm. As PHM cores become water-filled, their refractive indices become similar to water and they appear transparent. (*I*) Quantification of the relative percentages of gas- and fluid-filled PHMs following a 5-min rehydration period. (Scale bars: 10 μm.)

that results from the differences in the refractive indices of air and water (Fig. 3 *C* and *E*, and Fig. S3). However, water quickly began to permeate the shells capillary network within minutes (i.e., the core shell begins to transition from dark to light under optical microscopy; Fig. 3 *D* and *F*). Once water enters the particle core, the fate of the gas core is dependent on the surface pore diameter. When the mean surface pore diameter was ≤250 nm (i.e., formulations 2–4) the gas core rapidly dissolves (Fig. 3*G*). On the contrary, when the diameter exceeds 1.4 μm, free gas bubbles are released, although it is important to note that this is only observed in formulation 1 at a frequency of ∼6% (Fig. 3*H*). The number of water-filled PHMs after a 5-min rehydration period is 91.4 ± 4.5%, 71.9 ± 6.7%, and 93.9 ± 1.7% for formulations 1, 3, and 4, respectively; compared with 53.9 ± 7.1% for formulation 2 (Fig. 3*I*). Despite variable shell thickness, formulations 1, 3, and 4 all possess a single layer of transmural nanopores, whereas formulation 2 has a thick shell composed of a highly tortuous and heterogenous capillary network (Fig. 2). These results suggest that the filling rate is at least partially dependent on the tortuosity of the shell.

Permeation of water through the PHM shell was unexpected and is most likely due to the hydrophilic nature of the capillary network. Recall that, during fabrication, F-68, a nonionic triblock copolymer composed of a central hydrophobic chain of polyoxypropylene flanked by two hydrophilic chains of polyoxyethylene (PEO), is used to generate nanoemulsions within the PLGA shell. Removal of these droplets yields an F-68–coated capillary network with exposed PEO moieties, which increases the wettability of the channels and drives the unidirectional wicking of water into the PHM shell (Fig. 4) (27). At short time intervals (i.e., within minutes of rehydration), wicking produces menisci within the capillary channels, which, in turn, produces a gas–water interface (Fig. 4). In the presence of an oxygen gas sink (e.g., relatively hypoxic water or plasma), this interface should enable diffusion of the gas out of the PHM and into the bulk fluid. Therefore, the initial kinetics of O_2 release should correlate with the hydration rate of the PHM shell (i.e., a large burst release of O_2 should occur within 1 min of exposure to sink conditions). At longer timescales (i.e., 5- to 10-min posthydration), wicking drives dissolution of the gas core to yield fluid-filled particles (Fig. 4). It is important to note that, in the absence of a sink, dissolution of the gas core would be expected to be limited due to the poor solubility of O_2 in plasma.

To confirm that O_2 release from PHMs was diffusion controlled, we desaturated donated human red blood cells (hRBCs) with nitrogen gas and maintained them under stagnant conditions in an airtight water-jacketed (37 °C) reaction vessel equipped with a stir bar and an oximetric probe (16–19). The latter enabled the real-time continuous monitoring of oxyhemoglobin concentration (Fig. 5*A*). After a 30-min baseline, oxygen-loaded PHMs (i.e., interior gas core was 100% O_2) were added to the reaction vessel and monitored for two additional 30-min periods. Mixing was initiated during the second 30-min period. The observed oxyhemoglobin saturation (SO_2) increased within seconds of the addition of PHMs and remained constant over the entire 30-min period (Fig. 5*B*). During this time, PHMs quickly creamed to the top of the reaction vessel and saturated the surrounding blood (pO_2 = 740 mmHg; Fig. 5*A*). Not surprisingly, this saturation zone effectively removed the sink condition and created a barrier to further O_2 release. Further away from the saturation zone, SO_2 decreased, which explains the observed ΔSO_2 of only 20% (i.e., oximetric probe was placed at the interface of the saturated and desaturated zones; Fig. 5*A*) before initiation of mixing. Interestingly, the majority of PHMs remain gas-filled for the initial 30-min period. This is in agreement with our hypothesis and confirmed that sink conditions are required to drive O_2 release. Upon mixing, the sink condition was restored and the SO_2 increased ∼40% within seconds and was at ∼75% by the end of the second 30-min observation period. All PHMs tested were fluid-filled at the end of the second observation period. To determine whether the release kinetics varied among

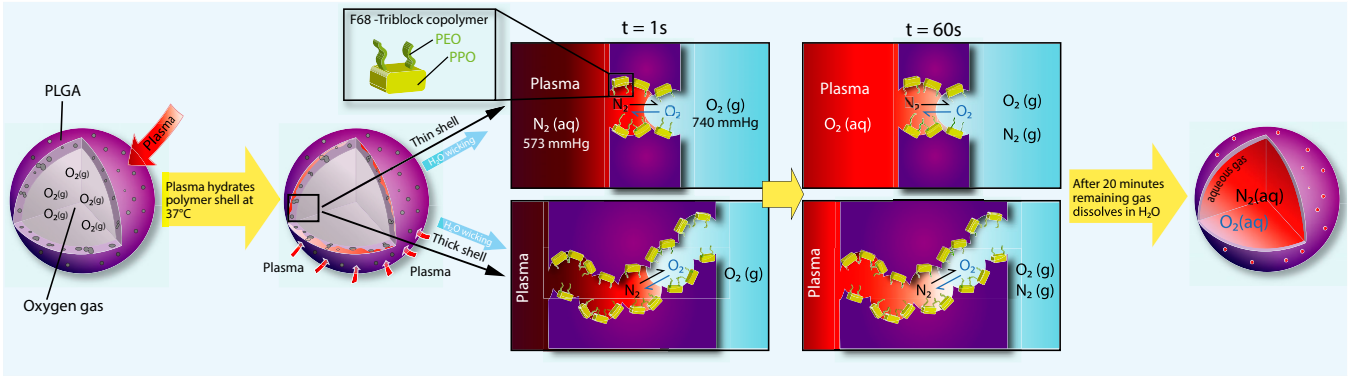

Fig. 4. Schematic representation of the proposed mechanism of oxygen release from PHMs. The capillary channels within the PLGA shell are rendered hydrophilic due to adsorbed F-68. Within seconds of rehydration, water is wicked into the capillary channels and creates a gas–water interface. In the presence of a sink, oxygen release from the PHM core occurs at the oxygen–water interface and is driven by differences in the partial pressure of oxygen. This process is identical to the mechanism of gas exchange in the lungs. After longer times, the wicking process leads to dissolution of the gas core and completes oxygen release from the PHMs (i.e., PHMs are 100% fluid filled). It is important to note that, in the absence of a sink, the poor solubility of oxygen in water arrests the wicking process and PHMs remain oxygen filled.

formulations, we converted the ΔSO_2 to fractional oxygen delivered (*SI Calculations*, *Calculation of Fractional Oxygen Released*) (19, 28). As expected, the bulk of the O_2 payload was released upon mixing, with ~85%, 83%, 78%, and 76% of oxygen release occurring within the first minute for formulations 1–4, respectively. Oxygen release continued for an additional 20 min, but at a much slower rate (Fig. 5*C*). This occurs because O_2 is continually released under constant sink conditions (i.e., deoxyhemoglobin is always in excess), which reduces the O_2 concentration gradient between the oxygen core and surrounding plasma, and hence, the driving force for O_2 diffusion out of the PHM core. This behavior is expected for diffusion-mediated processes and further supports our proposed mechanism of O_2 release. Note that shell thickness did not affect the kinetics of O_2 release on a macroscopic scale. This is not surprising, because O_2 release only requires hydration of the shell, a process that occurs independent of shell thickness. However, the density of transmural capillaries is expected to affect the release kinetics, with higher densities providing more surface area leading to faster release. Although technical limitations prevented us from directly quantifying this variable, our kinetic data suggest that the fractional oxygen release is similar for all PHMs. This suggests that PHMs have similar surface area available for gas transport.

Next, we characterized the gas carrying capacity of PHMs using a similar in vitro experimental setup as described above. Briefly, PHMs containing varying amounts of oxygen were added to the reaction vessel containing desaturated donated human blood, and the absolute ΔSO_2 was monitored after a 60-min observation period. The ΔSO_2 was subsequently converted to total volume of O_2 delivered (*SI Calculations*, *Calculation of Oxygen Carrying Capacity of Blood from SO_2*) (19, 28).

To determine the oxygen carrying capacity, the total volume of O_2 delivered was plotted as a function of PHM mass (Fig. 5*D*). Regression analysis revealed formulations 1–4 carried ~1.3 ± 0.05, 0.96 ± 0.21, 0.56 ± 0.08, and 0.88 ± 0.09 mL O_2/g PHM, respectively. By comparison, hRBCs only contain ~0.17 mL O_2/g RBC (*SI Calculations*, *Calculation of the Actual Oxygen Carrying Capacity of Blood per Gram of hRBC*). To confirm that PHMs completely delivered their gas payload, the volume of O_2 bound was plotted against the volume of O_2 administrated (Fig. 5*E*). Based on linear regression analysis, formulations 1–4 delivered ~59%, 88%, 89%, and 90% of their oxygen payload, respectively (Fig. 5*E*). Recall that formulation 1 released free gas bubbles upon rehydration, which explains the low correlation between bound and administered O_2. It is also interesting to note that formulation 4 has a similar gas carrying capacity as formulations 1 and 2 despite having an internal volume that is 7.5 times smaller. This is because formulation 4 contains 2.4×10^{11} #particles/g, compared with formulations 1 and 2, which only contain 6.2×10^9 and 3.0×10^9 #particles/g, respectively. As such, formulation 4 requires ~80 times the number of particles to deliver the same volume of gas as formulations 1 and 2.

Given its high gas carrying capacity and favorable size distributions, formulation 4 was evaluated for its ability to raise blood oxygen content in vivo, for its effects on pulmonary vascular resistance, and for blood compatibility. To quantify in vivo oxygen release, PHMs were injected into the femoral vein [which had an average oxyhemoglobin saturation (SO_2) of 50%] of male

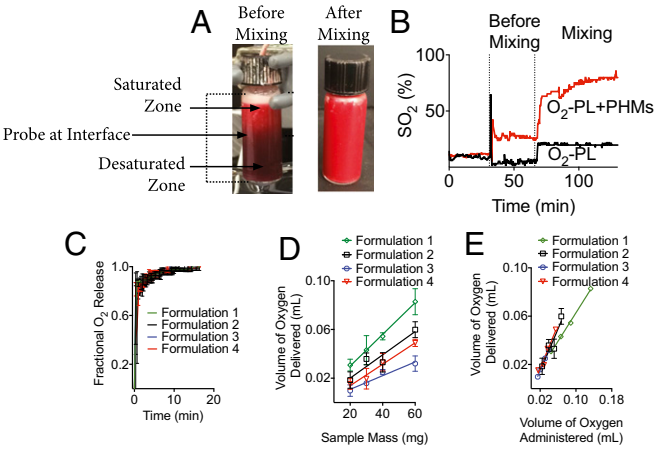

Fig. 5. PHMs readily deliver their oxygen payload when exposed to low oxygen tensions. (*A* and *B*) Addition of PHMs to desaturated blood under stagnant conditions increased the SO_2 by 20%. However, PHMs quickly creamed to the top of the reaction vessel and saturated the surrounding plasma, which removed the sink condition and arrested further oxygen release from PHMs. Upon mixing, the sink condition was restored and the SO_2 increased ~40% within seconds and was at ~75% by the end of the observation period. Increased blood oxygen saturations were also confirmed visually as a reddening of the sample from dark maroon to bright red. (*C*) Oxygen release kinetics was rapid for all formulations tested (T = 37 °C and rpm = 1,400) (Heidolph North America; Elk Grove Village, IL; model: MR Hei-Tec). (*D*) The oxygen carrying capacity of PHMs increased linearly with the quantity of PHMs delivered. (*E*) Formulations 2–4 deliver the majority of their gas payload, whereas formulation 1 only delivers ~60% of its oxygen carrying capacity. Data points on all plots represent the mean ± SEM.

Sprague–Dawley rats. Venous oxygen tension was measured continuously in the pulmonary artery (PvO_2) using an implantable oxygen electrode (Oxford Optronix). This model is clinically relevant in that the mechanism by which patients with airway or lung disease become hypoxemic is intrapulmonary shunting—instead of becoming reoxygenated in the lungs, blood passes from the pulmonary artery to the pulmonary vein (and subsequently the body) without gas exchange, creating arterial hypoxemia. Anesthetized rodents were intubated and instrumented for real-time continuous hemodynamic monitoring (Fig. S4). The average hemoglobin was ~9.0 g/dL and the FiO_2 was set at 0.3. Following a baseline period, oxygen-saturated Plasma-Lyte A suspensions containing 0% (control), 1% or 2% (wt/wt) PHMs [loaded with 100% (vol/vol) O_2 gas] were hand-injected into the femoral vein over 60 s. PvO_2 increased following injection, peaking between 100 and 200 s following the infusion and returning to baseline within 6–8 min (Fig. 6*A*). The peak change in PvO_2 (change from baseline) increased linearly with increasing PHM concentration (Fig. 6*B*). More specifically, solutions containing 1% and 2% (wt/wt) PHMs increased the PvO_2 by 12.8 ± 0.5 and 18.2 ± 3.4 mmHg, respectively, significantly more than did controls. Subtracting out the contributions of oxygenated Plasma-Lyte A (given in controls), we estimate that administration of 1% and 2% (wt/wt) PHMs increased the SvO_2 by ~15% and 30%, respectively, a clinically important quantity. This demonstrates the in vivo efficacy of PHMs as a one-way oxygen carrier. In these same animals, cardiac index (CI) was measured continuously using a ventricular conductance catheter, and was found to transiently increase during the injection, a change that is clinically desirable and related to volume administration (Fig. 6*C*). Similarly, pulmonary vascular resistance (PVR) decreased during injection and returned quickly to baseline (Fig. 6*D*), suggesting that the PHMs did not cause pulmonary vascular obstruction, and may have had a vasodilatory effect on the pulmonary vasculature due to the presence of oxygen. This is also a clinically very desirable effect.

To determine PHM blood compatibility, PHMs of varying concentrations (0.5, 1, 5, 10, and 20 mg/mL) were incubated with freshly isolated hRBCs for 5, 30, or 60 min and the concentration of cytoplasmic lactate dehydrogenase (LDH) determined using a LDH detection assay (Sigma). hRBCs suspended in water or Plasma-Lyte A were included as positive and negative controls, respectively. LDH levels were significantly lower than the positive control and similar to negative controls for all PHM concentrations and exposure times tested (Fig. 6*E*). These results clearly suggest that PHMs are not hemolytic.

Last, we characterized the long-term stability of PHM powders during prolonged storage under ambient conditions. This is important because long-term storage of PLGA-based particles can result in plasticization of the PLGA. This can lead to particle deformation, aggregation, and hydrolysis of the polyester backbone (29). We used PHM size distribution and gas carrying capacity as surrogates of PHM stability. Following storage for 60 d [days postfabrication (dpf)] at room temperature, we found no significant changes in size distributions ($d_{dpf0} = 1.3 \pm 1.0$ vs. $d_{dpf60} = 1.2 \pm 1.1$; Fig. S5*A*) or gas carrying capacity ($\Phi_{dpf0} = 0.81 \pm 0.05$ vs. $\Phi_{dpf60} = 0.76 \pm 0.14$, $P > 0.05$; Fig. S5*B*) of formulation 4. This suggests that dry storage of PHMs for 60 d at 25 °C minimized the effects of plasticization, thereby preserving the size distribution and gas carrying capacity of PHMs.

In conclusion, we have demonstrated fabrication of a polymer-based gas delivery agent for rapid administration of oxygen gas. Nanoporous PLGA-based hollow microparticles were fabricated from preformed polymers using a phase separation/self-emulsification strategy. PHM diameter, shell thickness, and porosity were controlled by varying the homogenization speed and PLGA precipitation rate. The oxygen carrying capacity was dependent on the volume of the core as well as the number of PHMs per gram. Oxygen loading and release into PHMs powders was achieved by passive diffusion through the nanoporous shell. Release was dependent on the hydration rate of the PLGA shell. PHMs became fluid-filled within 20 min of rehydration due to the hydrophilic nature of capillary network, which wicks water into the PHM and dissolves the gas core. Rapid i.v. infusion of oxygen-loaded PHMs was safe, and a single bolus was able to increase the PvO_2 for almost 10 min. Finally, storage of PHMs under ambient conditions does not affect particle size distribution or oxygen carrying capacity over a 2-mo period.

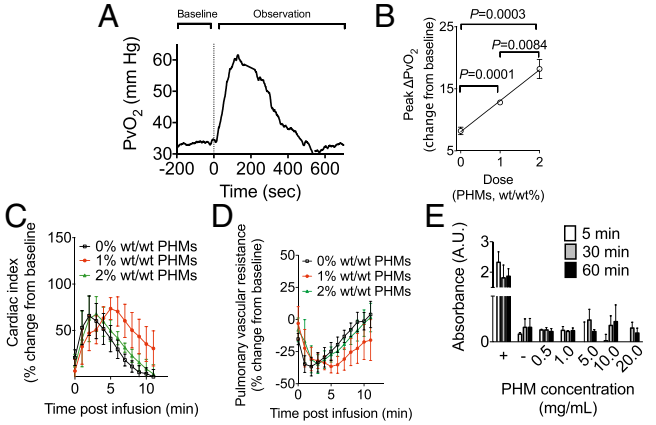

Fig. 6. PHMs rapidly increase blood oxygen content following i.v. injection. (*A* and *B*) Bolus infusions of oxygen-loaded PHMs transiently increased the PvO_2 (*A*) in a dose dependent manner (*B*). Infusion of oxygen-loaded PHMs [1% and 2% (wt/wt)] delivered significantly more oxygen gas than oxygen-saturated Plasma-Lyte A alone ($P = 0.001$ and 0.0084, respectively). (*C* and *D*) The cardiac index (CI) (*C*) transiently increased while the pulmonary vascular resistance (PVR) (*D*) decreased following infusion of oxygen-saturated Plasma-Lyte A or oxygen-loaded PHMs [1% and 2% (wt/wt)]. (*E*) PHMs were not hemolytic when incubated with freshly isolated hRBCs for up to 1 h at PHM concentrations of up to 20 mg/mL. Data points on all plots represent the mean ± SEM.

Materials and Methods

A list of materials and detailed information on particle characterization, quantification of porosity and shell thickness, swelling experiments, differential scanning calorimetry, instrumentation of animals for in vivo experiments, hemolysis assay, determination of cardiac index and pulmonary vascular resistance, and calculations of oxygen carrying capacity of blood and fractional oxygen release can be found in *Supporting Information*.

Preparation of PHMs. PHMs were manufactured using a solvent evaporation/self-emulsification process. The oil phase was prepared by dissolving 389 mg of PLGA, 471 μL of PFOB, and 54 mg of F-68 in 15.6 mL of DCM at room temperature. The oil phase was then added to a PVP solution (0.5 wt%, 80 mL) and immediately emulsified using a high-speed homogenizer (Silverson Verso; Silverson Machines). The emulsion was subsequently added to either 1.25 or 2.75 L of water, mixed at 200 rpm (Heidolph North America; Elk Grove Village, IL; model: MR Hei-Tec), and allowed to ripen overnight. PHMs were concentrated by gravitational settling, resuspended in a polyvinyl alcohol (PVA) solution (0.2 wt%), and mixed overnight at room temperature. PHMs were then removed from the PVA solution by centrifugation, resuspended in water, and freeze dried. All manufacturing conditions are listed in Table S1.

Time-Lapse Optical Microscopy. Dilute solutions of air-filled PHMs were prepared in air-saturated ultrapure water (1–5 mg/mL). A 10-μL droplet was added to a glass coverslip and placed in the fume hood. During the drying process, the PHMs creamed to the top of the droplet. The concentration was varied until a monolayer of PHMs was achieved after drying. The film was allowed to air dry for 1 h at room temperature. Rehydration experiments were performed on an Olympus IX71 fluorescent microscope equipped with a CCD camera (Qimaging RETIGA 2000R Fast B94) and various objectives (Uplan FLN 60×/1.25 Oil and Olympus PlanN 10×/0.25). Data acquisition and analysis were

performed using Metamorph. Glass coverslips containing the PHM thin films were mounted on the microscope and manually focused. Rehydration was accomplished by addition of a 10-μL droplet of air-saturated ultrapure water. Time-lapse images were acquired every second for 60 s and then every 30 s for an additional 4 min. At the end of the 5-min hydration period, low-magnification images (16×, five per sample) were taken and the relative percentage of gas and fluid-filled particles quantified.

Gas Release Kinetics. Gas release kinetics from PHMs was tested using the oxygen–hemoglobin transport system. PHMs powders (60 mg) were loaded with oxygen gas (100%) by passive diffusion under slight positive pressure and resuspended in oxygen-saturated Plasma-Lyte A solution (0.5 mL). Oxygen-saturated Plasma-Lyte A solutions were prepared by bubbling pure oxygen gas into Plasma-Lyte A until the pO_2 reached 740 mmHg. Oxygen saturations (SO_2) were continuously monitored using an oximetric monitoring system (Vigileo Monitor and PediaSat oximetry catheters; Edward Lifesciences). Donated human blood (hemoglobin, ∼6.2 g/dL; pH 7.3; T = 25 or 37 °C) was desaturated using a nitrogen/carbon dioxide gas mixture (95:5) to an oxyhemoglobin saturation of ∼15%. Baseline hemoglobin, oxyhemoglobin saturation, and oxygen tension were quantified (Radiometer ABL 80 Co-Ox Flex) and used to calibrate the oximetric catheter. Aliquots of desaturated human blood were placed into the oximetric monitoring system, and the baseline SO_2 was monitored for 30 min before each experiment. After 30 min, the desaturated blood was slowly added to the PHMs, and the SO_2 was monitored for 30 min with no mixing followed by an additional 30 min with mixing at 1,400 rpm (Heidolph North America; Elk Grove Village, IL; model: MR Hei-Tec). At the conclusion of each experiment, the hemoglobin, oxyhemoglobin saturation, and oxygen tension were measured and used to calculate the volume of oxygen delivered. Control experiments were conducted in a similar manner but without PHMs.

Dose–Response Measurements. Dose–response measurements were conducted using a similar experimental protocol as described above with the following exceptions: (*i*) PHM concentrations varied between 10 and 100 mg; (*ii*) resuspended PHMs were used immediately; (*iii*) PHMs were rapidly added to the desaturated blood in the oximetric monitoring system and immediately stirred at 1,400 rpm (Heidolph North America; Elk Grove Village, IL; model: MR Hei-Tec); (*iv*) SO_2 measurements continued until the absolute change between measurements was less than 5%.

In Vivo Animal Experiments. All procedures were approved by the Institutional Animal Care and Use Committee at Boston Children's Hospital. Male Sprague–Dawley rats (∼500 g; $n = 5$; Charles River Laboratories) were anesthetized [inhaled isoflurane, 2% (vol/vol), followed by i.p. ketamine, 80 $mg{\cdot}mL^{-1}{\cdot}kg^{-1}$, and xylazine, 10 $mg{\cdot}mL^{-1}{\cdot}kg^{-1}$] and orally intubated (14-gauge angiocatheter). Mechanical ventilation (SAR-1000; CWE) was maintained with a tidal volume of 10–12 mL/kg, positive end-expiratory pressure between 3 and 5 cmH_2O, peak inspiratory pressure of 20 cmH_2O, and FiO_2 of 1.0. Anesthesia was maintained with inhaled isoflurane [1.0–2.5% (vol/vol)] for the duration of the experiment. Animal temperature was maintained at 37 °C using a heating plate and closed-loop temperature control system (Physitemp; TCAT-2LV controller; ADInstruments). Animals were instrumented to allow real-time monitoring of hemodynamic data (Fig. S4). Each animal received a bolus injection (5 mL) of oxygenated Plasma-Lyte A via the venous line over 1 min, followed by a bolus of Plasma-Lyte A (1 mL) to flush the injection line. PvO_2 data were collected until it returned to baseline. This process was sequentially repeated for oxygen-loaded PHMs [1% and 2% (wt/wt)] resuspended in oxygen-saturated Plasma-Lyte A.

Hemolysis Assay. All procedures were approved by the Institutional Review Board (IRB) at Boston Children's Hospital. Venous blood was collected from healthy volunteers in tubes containing heparin (17 μL/mL), washed, and resuspended with Plasma-Lyte A (four parts hRBC to six parts Plasma-Lyte A). PHMs (0.5–20 mg/mL) were added to stock RBC solutions and incubated at 37 °C with gentle rocking, and the concentration of free LDH determined using the LDH-based TOX-7 kit (Sigma-Aldrich) according to the manufacturer's instructions.

ACKNOWLEDGMENTS. This work was supported by the Office of the Assistant Secretary of Defense for Health Affairs through the Peer-Reviewed Medical Research Program under Award W81XWH-15-1-0544. Furthermore, this work was supported by a DRIVE grant from the Boston Biomedical Innovation Center (NIH Grant U54HL119145), Smith Family President's Innovation Fund, Technology Development Grant from Boston Children's Hospital, and the Hess Family Foundation.

1. Bowen BD, Carmer ME (1926) The effect of a standard exercise upon the oxygen consumption of normal, overweight, and chronically ill individuals. *J Clin Invest* 2(4):299–313.
2. Sergi G, et al. (2010) Resting VO_2, maximal VO_2 and metabolic equivalents in free-living healthy elderly women. *Clin Nutr* 29(1):84–88.
3. Bourne G, Smith RG (1927) The value of intravenous and intraperitoneal administration of oxygen. *Am J Physiol* 82:328–334.
4. Tunnicliffe FW, Stebbing GF (1916) The intravenous injection of oxygen gas as a therapeutic measure. *Lancet* 188(4851):321–323.
5. Singh I, Rangoon MB, Shah MJ, Bombay MB (1940) Intravenous injection of oxygen under normal and atmospheric pressure. *Lancet* 235(6090):922–923.
6. Mik EG, et al. (2008) In vivo mitochondrial oxygen tension measured by a delayed fluorescence lifetime technique. *Biophys J* 95(8):3977–3990.
7. Stone GW, et al.; AMIHOT-II Trial Investigators (2009) Effect of supersaturated oxygen delivery on infarct size after percutaneous coronary intervention in acute myocardial infarction. *Circ Cardiovasc Interv* 2(5):366–375.
8. Sakai H, et al. (2004) Metabolism of hemoglobin-vesicles (artificial oxygen carriers) and their influence on organ functions in a rat model. *Biomaterials* 25(18):4317–4325.
9. Huang Y, et al. (2006) PEGylated albumin-heme as an oxygen-carrying plasma expander: Exchange transfusion into acute anemia rat model. *Biomaterials* 27(25):4477–4483.
10. Ortegon DP, et al. (2006) Bovine hemoglobin-based oxygen-carrying solution (HBOC-201) improves flap survival in a rat model of epigastric flap failure. *Microsurgery* 26(3):203–206.
11. Bauer J, et al. (2010) Perfluorocarbon-filled poly(lactide-co-gylcolide) nano- and microcapsules as artificial oxygen carriers for blood substitutes: A physico-chemical assessment. *J Microencapsul* 27(2):122–132.
12. Spiess BD (2009) Perfluorocarbon emulsions as a promising technology: A review of tissue and vascular gas dynamics. *J Appl Physiol (1985)* 106(4):1444–1452.
13. Alayash AI (2004) Oxygen therapeutics: Can we tame haemoglobin? *Nat Rev Drug Discov* 3(2):152–159.
14. Jia Y, et al. (2004) Oxygen binding and oxidation reactions of human hemoglobin conjugated to carboxylate dextran. *Biochim Biophys Acta* 1672(3):164–173.
15. Cabrales P, Friedman JM (2013) HBOC vasoactivity: Interplay between nitric oxide scavenging and capacity to generate bioactive nitric oxide species. *Antioxid Redox Signal* 18(17):2284–2297.
16. Kheir JN, et al. (2013) Bulk manufacture of concentrated oxygen gas-filled microparticles for intravenous oxygen delivery. *Adv Healthc Mater* 2(8):1131–1141.
17. Kheir JN, et al. (2012) Oxygen gas-filled microparticles provide intravenous oxygen delivery. *Sci Transl Med* 4(140):140ra88–140ra88.
18. Polizzotti BD, Thomson LM, O'Connell DW, McGowan FX, Kheir JN (2014) Optimization and characterization of stable lipid-based, oxygen-filled microbubbles by mixture design. *J Biomed Mater Res B Appl Biomater* 102(6):1148–1156.
19. Thomson LM, Seekell RP, McGowan FX, Kheir JN, Polizzotti BD (2016) Freeze-thawing at point-of-use to extend shelf stability of lipid-based oxygen microbubbles for intravenous oxygen delivery. *Colloids Surf A Physicochem Eng Asp* 500:72–78.
20. Kheir JN, et al. (2012) Administration of intravenous oxygen increases arterial oxygen content and cerebral oxygen delivery during CCC-only CPR. *Circulation* 126(Suppl 21):A206.
21. Talu E, Lozano MM, Powell RL, Dayton PA, Longo ML (2006) Long-term stability by lipid coating monodisperse microbubbles formed by a flow-focusing device. *Langmuir* 22(23):9487–9490.
22. Watanabe H, Suzuki M, Inaoka H, Ito N (2014) Ostwald ripening in multiple-bubble nuclei. *J Chem Phys* 141(23):234703–234707.
23. Yang W-H, Smolen VF, Peppas NA (1981) Oxygen permeability coefficients of polymers for hard and soft contact lens applications. *J Membr Sci* 9(1):53–67.
24. Ferenz KB, Waack IN, Mayer C, de Groot H, Kirsch M (2013) Long-circulating poly (ethylene glycol)-coated poly(lactid-co-glycolid) microcapsules as potential carriers for intravenously administered drugs. *J Microencapsul* 30(7):632–642.
25. Lensen D, Vriezema DM, van Hest JCM (2008) Polymeric microcapsules for synthetic applications. *Macromol Biosci* 8(11):991–1005.
26. Ben Henda M, Ghaouar N, Gharbi A (2013) Rheological properties and reverse micelles conditions of PEO-PPO-PEO Pluronic F68: Effects of temperature and solvent mixtures. *J Polym* 2013(1):1–7.
27. Chen H, Cogswell J, Anagnostopoulos C, Faghri M (2012) A fluidic diode, valves, and a sequential-loading circuit fabricated on layered paper. *Lab Chip* 12(16):2909–2913.
28. Nebout S, Pirracchio R (2012) Should we monitor $ScVO_2$ in critically ill patients? *Cardiol Res Pract* 2012(5):370697.
29. Sayin B, Calis S (2004) Influence of accelerated storage conditions on the stability of vancomycin-loaded poly(D,L-lactide-co-glycolide) microspheres. *FABAD J Pharm Sci* 29:111–116.